Journal of
Materials Chemistry A

Materials for energy and sustainability

Accepted Manuscript

This article can be cited before page numbers have been issued, to do this please use: A. Bafekry, M. Obeid, C. Nguyen, M. Bagheri Tagani and M. Ghergherehchi, *J. Mater. Chem. A*, 2020, DOI: 10.1039/D0TA02847A.

ROYAL SOCIETY OF CHEMISTRY

rsc.li/materials-a

View Article Online
DOI: 10.1039/D0TA02847A

Journal Name

ARTICLE TYPE

Cite this: DOI: 10.1039/xxxxxxxxxx

Graphene hetero-multilayer on layered platinum mineral Jacutingaite (Pt_2HgSe_3): Van der Waals heterostructures with novel optoelectronic and thermoelectric performances

A. Bafekry[1,2†], M. M. Obeid[3], Chuong V. Nguyen[4], M. Ghergherehchi[5†], M. Bagheri Tagani[1]

Received Date
Accepted Date

DOI: 10.1039/xxxxxxxxxx

www.rsc.org/journalname

Motivated by the recent successful synthesis of layered platinum mineral jacutingaite (Pt_2HgSe_3), we have studied the optoelectronic, mechanical, and thermoelectric properties of graphene hetero-multilayer on Pt_2HgSe_3 monolayer (PHS) heterostructures (LG/PHS), by using first-principles calculations. PHS is a topological insulator with band gap about 160 meV with fully relativistic calculations and when graphene layers stacked on PHS, a narrow band gap opening $\sim$ 10-15 meV. In presence an gate-voltage and out-of plane strain i. e. pressure, the electronic properties is modified, the Dirac-cone of graphene can be shifted upwards (downward) to the lower (higher) binding energy. Absorption spectrum demonstrates two peaks, which are located around 216 nm (5.74 eV) and protracted to 490 nm (2.53 eV), indicating that PHS could absorb more visible light. Increasing the number of graphene layers on PHS has a positive impact on the UV-Vis light absorption and a clear red-shift with enhanced absorption intensity. To investigate the electronic performance of the heterostructure, electrical conductance and thermopower of a device composed of graphene layers and PHS is examined by combination of DFT and Green function formalism. Number of graphene layers can significantly tune thermopower and electrical conductance. Such analysis reveals that the heterostructuring not only significantly affect the electronic properties, but they also can be used as an efficient way to modulate the optic and thermoelectric properties.

1 Introduction

Following the successful exfoliation of graphene[1], a plethora of theoretical and experimental studies have been conducted to investigate its remarkable physical properties and potential applications[2–4]. These findings show that graphene possesses many intriguing physical properties, such as high carrier mobility and conductivity[4,5] that make it promising candidate for various applications in high-efficiency nanodevices, such as field-effect transistors (FETs)[6], and photodetectors[7]. However, before using graphene in practical applications, it is important to potentially solve its drawback, that is to open a sizable band gap at Dirac cone of graphene. It is obvious that the lack of a band gap in graphene hinders its potential applications in high-speed devices, such as FET[8]. Recently, in parallel with graphene studies, the research community has also been focusing on other graphene-like two-dimensional materials (2DM)[9,10]. Up to date, many different graphene-like 2DM have been synthesized experimentally and predicted theoretically, such as transition metal dichalcogenides[11,12], phosphorene[13,14], silicene[15]. These studies demonstrated that owing to the extraordinary properties, 2DM can be considered as promising candidate for electronics, spintronics and optolectronics[16–18].

Recently, layered platinum mineral jacutingaite (Pt_2HgSe_3), a new kind of platinum group minerals was discovered firstly by Cabral et al[19]. The crystal structure of Jacutingaite has also been

[1] *Department of Physics, University of Guilan, 41335-1914 Rasht, Iran*
[2] *Department of Physics, University of Antwerp, Groenenborgerlaan 171, B-2020 Antwerp, Belgium*
[3] *Department of Ceramics, College of Materials Engineering, University of Babylon, 51002, Hilla, Iraq*
[4] *Department of Materials Science and Engineering, Le Quy Don Technical University, Ha Noi 100000, Vietnam.*
[5] *College of Electronic and Electrical Engineering, Sungkyun kwan University, Suwon, Korea*
† *To whom correspondence should be addressed. Email: Bafekry.asad@gmail.com; and mitragh@skku.edu*

View Article Online
DOI: 10.1039/D0TA02847A

defined through powder X-ray diffraction and its layered character is supported by the experimental reports[20]. The *PHS* has been predicted recently as a large band gap quantum spin Hall (QSH) insulator[21] and its Fermiology under electron and hole doping suggests the unconventional superconductivity[22]. The QSH state in *PHS* has been experimentally demonstrated using scanning tunneling microscopy (STM)[23]. On the other hand, it is found that few nanometers thick as well as bulk jacutingaite is stable under ambient conditions on a timescale of months and even to a year[23]. Similar to graphene, Jacutingaite also exhibits a gapless semiconductor without considering spin-orbit coupling (SOC). It leads to the existence of an important question that is whether the Jacutingaite can be considered as a potential material for designing future high-performance nanodevices and whether its band gap can be tuned. It is interesting that the electronic properties, including band gap values and band edges of 2DM can be adjusted by different common strategies, such as strain engineering[24–26], electric field[27] or thickness layers[28–31]. Giovannetti et al.[28] showed that the layer effect can be used to open a band gap of 53 meV in graphene. More interestingly, the scientific community has also focused on the formation of van der Waals heterostructures by placing different 2DM on top of each other. Up to date, a plethora of heterostructures, especially graphene-based heterostructures have been fabricated experimentally and predicted theoretically, such as graphene/TMDs[32,33], graphene/GaS(Se)[34,35,37,38], graphene/phosphorene[38,39]. Aziza and his co-workers[37] showed that the Dirac cone of graphene can be shifted upwards to the lower binding energy when it stacked on GaSe thin film. On the other hand, Phuc et al.[38] theoretically predicted that both the band gap and band alignment in the Graphene/GaSe heterostructur can be adjusted by external electric field or strain. It is well known that the electronic properties of 2DM can be tuned by applying strain or external electric field and mechanical strain[40–43]. [40–50] The controllable structural and electronic properties of above graphene-based HTSs make them suitable for fabricating novel nanodevices. Therefore, knowledge of the structural and electronic properties of *PHS* along with the effects of graphene heterostructuring is extremely important towards its future applications. In this work, using first-principles calculations, firstly we investigate the structural, electronic, optical and thermoelectric properties of *PHS* and graphene layers on *PHS*. In the *LG*/*PHS*, the electric field and out-of-plane strain is also considered in calculations to change its electronic properties. Our results show that by applying an gate-voltage and pressure, the electronic structure of *LG*/*PHS* can be significantly modified.

2 Methods

The electronic structure is calculated with geometric optimization using density functional theory (DFT) as implemented in the OpenMX Package[51]. This code finds the eigenvalues and eigenfunctions of the Kohn-Sham equations self-consistently using norm-conserving pseudopotentials[52], and pseudoatomic orbitals (PAOs)[53,54]. In addition, we used the Perdew-Burke-Ernzerhof generalized gradient approximation (GGA) for exchange and correlation[55]. After convergence tests, we choose an energy cutoff of 400 Ry so that the total-energy converges below 1.0 meV/atom. In the first step, the atomic positions are optimized using a quasi-Newton algorithm for atomic force relaxation. The geometries were fully relaxed until the force acting on each atom was less than 1 meV/Å. The Brillouin zone (BZ) is sampled by a **k**-mesh grid of $23 \times 23 \times 1$ and scaled according to the size of the supercell by using the Monkhorst-Pack scheme[56]. The *PHS* is modelled as a periodic slab with a sufficiently large vacuum layer (20 Å) in order to avoid interaction between adjacent layers. In order to accurately describe the van der Waals (vdW) interaction in *PHS*, we adopted the empirical correction method presented by Grimme (DFT-D2)[57], which has been proven reliable for describing the long-range vdW interactions. The vibrational properties were obtained from the small displacement method as implemented in the PHON code[59]. Using this method, the phonon frequencies were calculated at the Γ point of the BZ.

In order to compute electrical conductance and thermopower of the heterostructures, a combination of DFT approach and Green function formalism is used. First, we construct an orthorhombic unit cell and repeat it along Y-direction 3 times. Then, tow semi-infinite electrodes are attached to the central region to make a device composed of graphene and (Name of structure) monolayer. Density matrix is calculated using Green function formalism and periodic boundary condition along X-direction and dirichlet one along Y-direction for solving Poisson equation. All calculations are performed using SIESTA package[58] with a double-zeta polarized basis set. Cut-off energy is set $120H$ and a 10×50 k-point sampling is used to map reciprocal lattice. The transmission coefficient of the device is calculated by $T_e = [G^R(E)\Gamma_L(E)G^A(E)\Gamma_R(E)]$ where $\Gamma^R(A)$ and $\Gamma_L(R)$ denotes retarded (advanced) Green function and left (right) electrode broadening function, respectively. Thermopower and

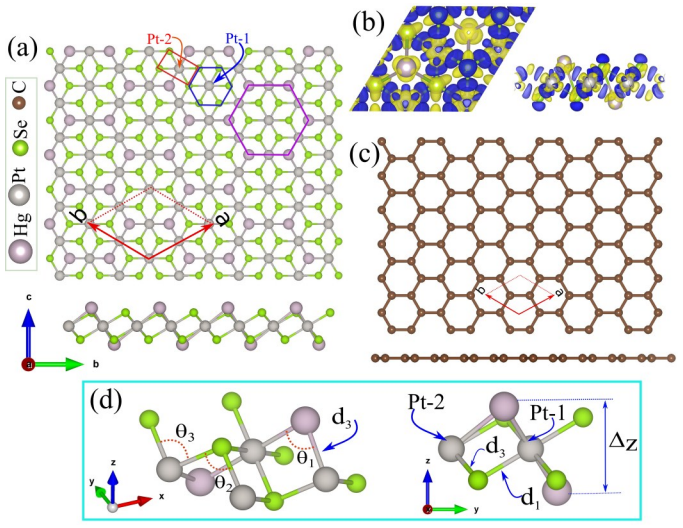

Fig. 1 Geometric atomic structure of (a) *PHS* monolayers, with its hexagonal primitive unit cell indicated by the red parallelogram. (b) Difference charge density is shown in the inset. Blue and yellow regions represent charge accumulation and depletion, respectively. (c) Geometric atomic structure of Graphene. (d) Schematic view of PHS structure with structural parameters.

View Article Online
DOI: 10.1039/D0TA02847A

electrical conductance of the device is calculated in the linear response regime as follows: $S = \frac{L_1}{eTL_0}$, $G = e^2L_0$, Where $L_n = \frac{2}{h}\int dE(E-E_f)^n T_e E(-\frac{\partial f(E)}{\partial E})$ and also $f(E) = (1+exp((E-E_f)/k_BT))^{-1}$ is Fermi distribution function.

3 Pristine monolayers

The geometric atomic structure of *PHS*, with its hexagonal primitive unit cell, is shown in Fig. 1(a). The hexagon of *PHS* lattice contains 12 atoms (4 Pt, 2 Hg and 6 Se) per primitive unit cell and with the trigonal space group P_{3m1} (No. 164). The crystal structure of Jacutingaite *PHS* forms a bipartite lattice with two sublattices[19] and the layered structure can be viewed as a $2 \times 2 \times 1$ supercell of 1T-$PtSe_2$ structure phase with additional Hg atoms that are placed in the anticubo-octahedral voids of Se atoms. The lattice constant of *PHS* is calculated to be 7.60 Å, while the bond lengths of Pt-Hg and Hg-Se are 2.8 Å and 3.74 Å, respectively. These results are listed in Table 1. We can see two type of Pt atoms in the *PHS* structure that indicate with Pt_1 and Pt_2, respectively and indicated in the inset in Fig. 1(a). The Pt_1 atom connects to six nearest Se atoms and forms Pt_1Se, 6 local octahedral coordination with Pt_1-Se bond length of 2.54 Å. While the Pt_2 atom constitutes Pt_2-Se, 4 square lattice with Pt_2-Se bond length of 2.46 Å, which is slightly smaller than the Pt_1-Se[19,20]. The Pt_1-Se bond length is 2.54 Å which is slightly larger than the Pt_2-Se bond length of 2.46 Å. The vertical distance between the two Hg and Se atomic planes is 3.49 Åand 2.60 Å, respectively. These results are in agreement with previous report[23].

The difference charge density ($\Delta\rho$) as shown in the inset (see Fig. 1(b)) is defined as:

$$\Delta\rho = \rho_{PHS} - \rho_{Pt} - \rho_{Hg} - \rho_{Se} \quad (1)$$

where ρ_{PHS}, ρ_{Pt}, ρ_{Hg}, and ρ_{Se} represents the charge densities of the PHS and isolated atoms, respectively. The blue and yellow regions represent charge accumulation and depletion, respectively. According to the charge transfer analysis, the charge of Pt, Hg and Se atoms are +0.182 *e*, +0.176 *e*, and -0.194 *e*, respectively. The Pauling electro-negativity values for Pt, Hg and Se atoms are 2.28, 2 and 2.55, respectively. A high charge density can be seen around the Se atoms, reflecting the electro-negativity character.

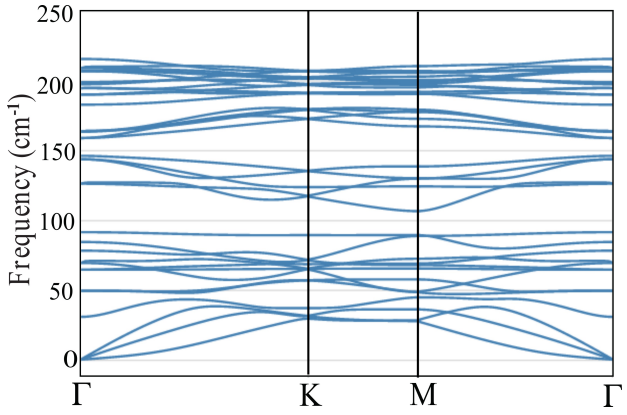

Fig. 2 The phonon band dispersion of *PHS*.

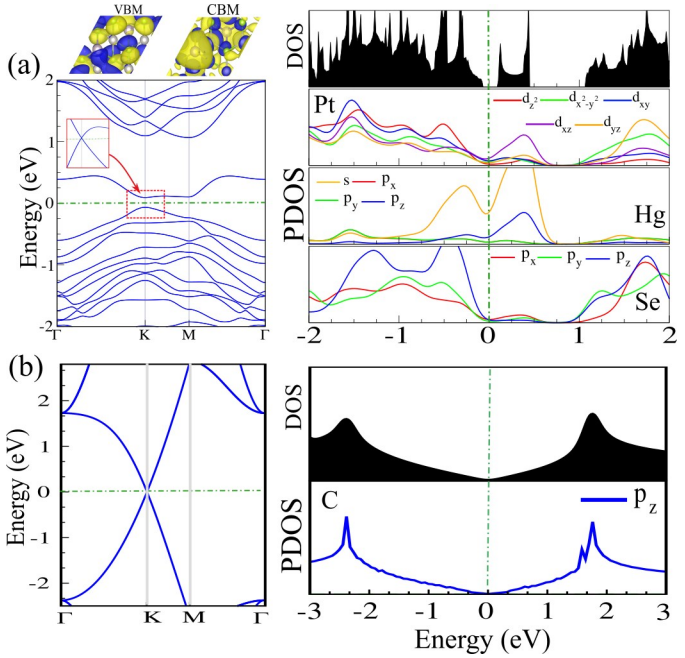

Fig. 3 Electronic band structure (left panel), density of state (DOS) and partial DOS (PDOS) (right panel) of (a) *PHS* with considering of spin-orbit coupling (SOC) and (b) Graphene monolayer. Zoom of the band structure without SOC indicated in the inset for *PHS*. The zero of energy is set to the Fermi level. Charge densities of valence band maximum (VBM) and the conduction band minimum (CBM) are shown in top panel of *PHS*. Blue and yellow regions represent charge accumulation and depletion, respectively.

This electro-negativity difference explains the electron transfer from Pt and Hg atoms to Se atoms. In Fig. 1(c) we depict the lattice structure, corresponding to hexagonal primitive unit cell (red parallelogram) of monolayer Graphene which has a planar structure with a lattice constant of $a = b = 2.46$ Å where the C-C bond length is $d_{CC} = 1.42$ Å and the C-C-C bond angle is equal to 120°[60]. The schematic view of *PHS* structure with structural parameters is shown in Fig. 1(d).

Cohesive energy, which is defined as the energy required to separate condensed material into isolated free atoms, is one of the most important physical parameters in quantifying the stability of materials. The cohesive energy per atom was calculated using the following equation:

$$E_{coh} = (E_{Pt} + E_{Hg} + E_{Se}) - E_{PHS}/n_{tot} \quad (2)$$

where E_{Pt}, E_{Hg} and E_{Se} represents the energies of isolated single Pt, Hg and Se atoms. E_{PHS} and n_{tot} represents the total energy of the *PHS*, and total number of atoms, respectively. The cohesive energy of *PHS* is found to be 4.72 eV/atom. The dynamical stability of single-layers of *PHS* is verified by calculating their phonon band dispersions through the whole BZ which are presented in Fig. 2. Apparently, phonon branches are free from any imaginary frequencies indicating the dynamical stability of the free-standing *PHS*, which is consistent with the results of a previous studies[23].

In order to explain the electronic states and clarify the contri-

View Article Online
DOI: 10.1039/D0TA02847A

Table 1 The structural and electronic parameters of *PHS* shown in Fig. 1(d). The corresponding structural and electronic parameters including lattice constant **a**; the bond lengths between Pt(1,2)-Se atom ($d_{1,2}$), Pt-Hg atom (d_3); the bond angles between Hg-Pt-Hg θ_1, Pt-Se-Pt atoms θ_2 and Se-Pt-Se atoms θ_3; the thickness defined by the difference between the largest and smallest z coordinates of Hg atoms (Δz); the cohesive energy of, (E_{coh}); Electronic states (ES) are specified as topological insulator (TI). The band gap is shown in parentheses and is given in meV.

a (Å)	$d_{1,2}$ (Å)	d_3 (Å)	Δz (Å)	θ_1 (°)	θ_2 (°)	θ_3 (°)	E_{coh} (eV/atom)	ES (meV)
7.43	(2.57, 2.54)	2.8	3.44	85.27	96	95.4	4.72	TI (160)

butions from different orbitals, we calculated the electronic band structure, density of states (DOS) and partial DOS (PDOS), as shown in Fig. 3. Without spin-orbit coupling (SOC), the band structure of *PHS* shows a gapless semiconductor character with a linear band dispersion relation near the Fermi level. The massless Dirac fermions are found at the high-symmetry K point (see Fig. 3(a)). With considering of SOC effect, the Dirac-cone-like dispersion crossings without SOC at the high-symmetry K point is now gapped and a continuous band gap of 160 meV appears between the valence and conduction bands. The valence band maximum (VBM) and the conduction band minimum (CBM) are located at K points. The charge densities of VBM and the CBM are shown in top of Fig. 2(a). Blue and yellow regions represent charge accumulation and depletion, respectively. Our results are in agreement with previous calculation[23]. We can see from PDOS that, the VBM mainly contributed by Hg-s and Se-p_z atomic orbitals, while the CBM is derived from Pt-(d_{xz}) and Hg-s orbitals. Graphene is a semi-metal with a zero gap, while the valence and conduction bands crossing with linear dispersion. From the PDOS, it is known that C-p_z orbitals form bonding orbital (π) and anti-bonding orbital (π^*), touching at one point in the momentum space at the Fermi-level (see Fig. 3(b)).

4 Hetrostructures

Here after, the monolayer, bilayer and trilayer of graphene with Pt_2HgSe_3 (*PHS*) heterostructures, are labeled as *MLG*/*PHS*, *BLG*/*PHS* and *TLG*/*PHS*, respectively. We used a 3 × 3 supercell of graphene layers (a= b = 7.38 Å) on top of a 1 × 1 of *PHS* (a = 7.43 Å), which is benefit to forming stable structures. The lattice constant mismatch (δ) between top and bottom layer of two structures is defined as

$$\delta = \frac{|a_T - a_B|}{a_B} \times 100\%, \quad (3)$$

where a_T and a_B are the lattice constant of top and bottom layers, respectively. The value of lattice constant mismatch between *PHS* with graphene is small of about 2.2 %. Thus, relative to their free-standing states, there is no major distortion in the geometric structures of *PHS* and graphene due to lattice mismatch. To investigation the structural stability of *LG*/*PHS*, the most stable pattern are obtained by placing different stacking (AA and AB) of graphene layers on the *PHS* surface (see Fig. S1 in supplementary information). With fully structural optimization, we determine the most stable stacking as the minimum energy configuration among the different patterns. The binding energy (E_b) of the constructed heterostructures is calculated using the given formula as below[61]:

$$E_b = E_{tot} - E_{PHS} - nE_{Gr}/m \quad (4)$$

where E_b, E_{Gr} and E_{PHS} are the total energies of the optimized *nLG*/*PHS* HTSs, *PHS* monolayer, and graphene layers, respectively. The letter n represents the layer number of graphene and m is carbon atoms in the *Gr*/*PHS* hetero-multilayer. The binding energy as functions of interlayer distances for *MLG*/, *BLG*/ and *TLG*/*PHS* heterostructures is presented in Fig. 3. A negative value of binding energy emphasizes the thermodynamic stability of the constructed heterostructures[62]. Our results show that the minimum energy configuration of *MLG*/, *BLG*/ and *TLG*/*PHS* is AB-stacking arrangement, as shown in Fig. S1 of supplementary information. Under the equilibrium interlayer distance, a negative value of -78 meV is obtained for the constructed *MLG*/*PHS*, indicating that *PHS* and graphene could form thermodynamically stable van der Waals *MLG*/*PHS*. Note that equilibrium distance between *PHS* and graphene for *PHS*/*MLG* is 3.12 Å. The effect of increasing the numbers of graphene layers on the stability of heterostructures has also been evaluated. It is found that *TLG*/*PHS* stacking configuration with the binding energy of E_b = -78 meV is energetically more favorable than that of *BLG*/*PHS*, which has a binding energy of E_b= -72 meV. Therefore, these heterostructures are energetically stable and can be synthesized experimentally. The obtained results are in good agreement with the previous calculation on *$PtSe_2$/graphene* hetero-multilayer[61].

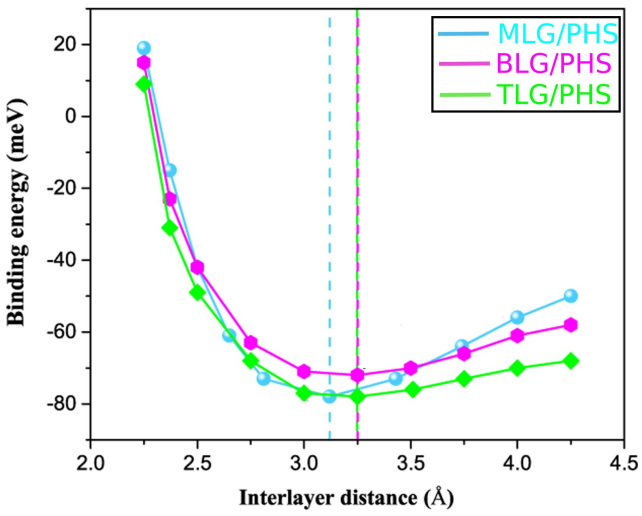

Fig. 4 The binding energy as functions of interlayer distances for *MLG*/*PHS*, *BLG*/*PHS* and *TLG*/*PHS* heterostructures.

View Article Online
DOI: 10.1039/D0TA02847A

Table 2 The structural and electronic parameters of LG/PHS heterostructures including lattice constant **a**; the bond lengths atoms ($d_{1,2,3}$), and bond length of C-C atoms in graphene layers (d_{CC}); the bond angles between ($\theta_{1,2,3}$); the thickness (Δz); the interlayer distance (h); All distance and angles are given in Å and °, respectively. The binding energy (E_{coh}); the charge transfer (ΔQ) between atoms; Electronic states (ES) are specified as semi-metal (SM) and semiconductor (SC). The band gap is shown in parentheses and is given in meV.

Sys.	**a**	$d_{1,2,3}$	$\theta_{1,2,3}$	δz	h	d_{CC}	E_b	ES
MLG/PHS	7.45	(2.55, 2.52, 2.81)	(82.65, 93.86, 93.26)	3.64	3.12	1.43	-78	SC (16)
BLG/PHS	7.45	(2.54, 2.52, 2.75)	(88.10, 94.13, 93.78)	3.68	3.25	1.43	-73	SM
TLG/PHS	7.45	(2.55, 2.52, 2.75)	(87.96, 94.13, 93.90)	3.69	3.25	1.43	-78	SM

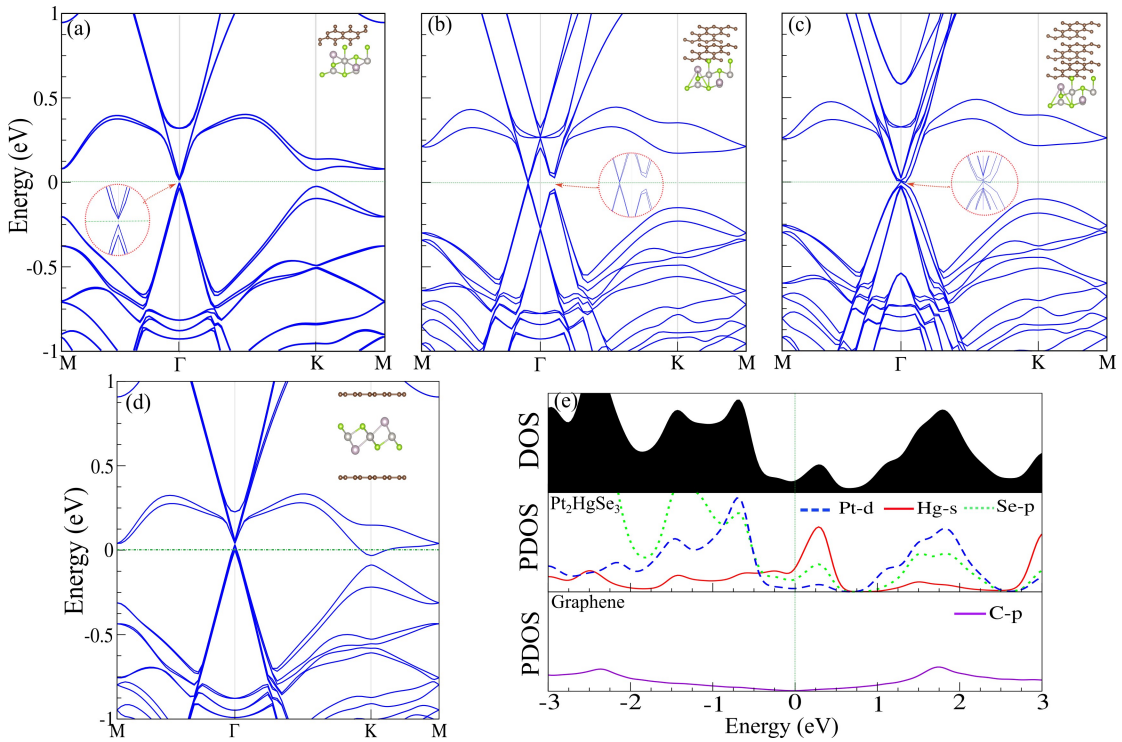

Fig. 5 Electronic band structure of (a) MLG/PHS, (b) BLG/PHS and (c) TLG/PHS HTS with considering of SOC. (d) $MLG/PHS/MLG$. The zero of energy is set at Fermi level. Optimized structures are shown in the inset. (e) DOS and PDOS of MLG/PHS.

The obtained parameters for the lattice constant (a), interlayer distance (Z_{eq}) and other parameters of the studied HTSs are listed in Table 2. The calculated lattice constants are equal to 7.45 Å, while the bond lengths d_1 and d_2 are determined to be 2.58 and 2.59 Å, respectively. The three angles in lattice of MLG/PHS are 121° (θ_1), 116° (θ_2) slightly deviating from 120°. The interlayer distance between PHS and different graphene layers are in the range of 3.13–3.33 Å, which is typical of vdW equilibrium spacing. In BLG/PHS, the lattice parameter is 7.45 Å, while the bond lengths are d_1 = 2.61 Å and d_2 = 2.62 Å. The bond angles are same $\theta_1 = \theta_1 = 119°$. Notice that the buckling (Δz) are determined to be 0.86 (in MLG) and 0.25 Å (in BLG). The lattice constant of TLG/PHS is calculated to be 7.45 Å. The bond lengths of Pt-Hg and Hg-Se are calculated 2.81 and 3.82 Å, respectively, which are slightly larger than that of pristine PHS. The interlayer distance between the two monolayer planes is 3.12 Å.

The electronic band structure of LG/PHS are displayed in Fig. 5. The optimized atomic structures of heterostructures are also depicted in the inset of Fig. 5(a-d). First, one can observe that when single layer graphene is placed on the PHS, there is a tiny band gap of 16 meV, opening at Dirac Γ point of graphene, as illustrated in the inset of Fig. 5(a). The nature of such band gap, opening in graphene is due to the sublattice symmetry breaking. However, it should be noted that such band gap opening in graphene is smaller than the thermal fluctuation k_BT of 26 meV at room temperature. Furthermore, we can find from Fig. 5(a) that the PHS part in the MLG/PHS possesses a semiconducting nature with a narrow band gap of 95 meV, forming between the VBM and CBM at the K point. In addition, to have a clear picture of the band alignment of MLG/PHS, in Fig. 5(e) we plot the DOS and PDOS of MLG/PHS. We can find that the VBM of PHS layer at K point is due to the hybridization of Pt-d and Se-p orbitals, while its CBM is contributed by the hybridization of Hg-s and Se-p orbitals, which confirms the semiconducting behavior.

The band structure of BLG/PHS with considering SOC effect is depicted in Fig. 5(b). Interestingly, we can find that in the presence of the SOC effect, the Dirac cone at Γ point of MLG splits into two different Dirac cones in the BLG/PHS heterostructure, as il-

View Article Online
DOI: 10.1039/D0TA02847A

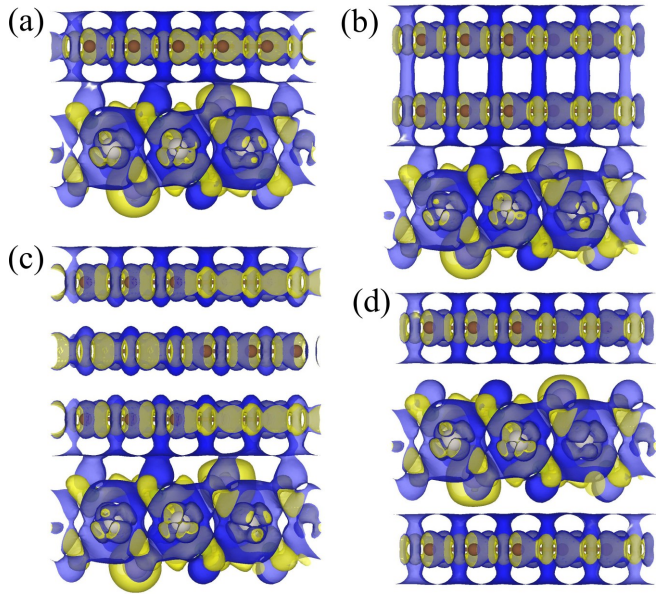

Fig. 6 Difference charge density of (a) MLG/PHS, (b) BLG/PHS, (c) TLG/PHS and (d) $MLG/PHS/MLG$ heterostructures. Blue and yellow regions represent charge accumulation and depletion, respectively.

lustrated in the inset of Fig. 5(b). The nature of band splitting is due to the Rashba band splitting across the interface due to internal electric field and a strong SOC effect in the lack of inversion inversion and time reversal symmetry[63]. One of the Dirac cones opens a tiny band gap of 5 meV, whereas other one has opened a band gap of 70 meV. Similar to the MLG/PHS, the PHS part in the BLG/PHS also exhibits a semiconducting feature. The band gap of PHS layer at K point in the BLG/PHS is still larger than that of PHS layer in the MLG/PHS. It indicates that the SOC band gap of PHS monolayer can also be modulated by changing the graphene thickness layer. In the case of TLG/PHS, the SOC band gap of of the PHS part is also opened at K point. The heterostructure in this case remains a semi-metal feature. When the PHS is sandwiched between two graphene layers, as depicted in Fig. 5(d), we find that the SOC band gap of PHS layer at K point is also occurred. The value of SOC band gap in this case is about 85 meV, which is smaller than that of the MLG/PHS. All the above mentioned suggests that the SOC band gap of PHS depends not only on the graphene thickness layers, but also on the positions of graphene stacking layers.

The difference charge density and a quantitative results of charge distribution of different heterostructures are shown in Fig. 6. The difference charge density Δ_ρ is defined as $\Delta_\rho = \rho_{LG/PHS}\text{-}\rho_{LG}\text{-}\rho_{PHS}$, where $\rho_{LG/PHS}$, ρ_{LG}, and ρ_{PHS} represents the charge densities of the LG/PHS heterostractures and free-standing graphene layers and PHS, respectively. The blue regions represent the charge accumulation, while the red areas denote the charge depletion. We can see that due to the interaction between two monolayer an charge redistribution occurs at the LG/PHS interface region. All these stacking of heterostructures exhibit a small charge transfer. The charge accumulation largely occurs in the central region of interface, and the charge depletion mostly stems from the two boundaries of interface.

5 Electric field and strain engineering

From the perspective of potential device applications, the ability to control topological electronic properties by controlling the Fermi-level via electric field (E-field) is highly desirable[64–67]. The existence of buckling in the PHS, leads to a potential difference between the two atomic sub-lattices, which turns out to potentially intrinsically useful in tuning the electronic properties in terms of a perpendicular E-field. We turn our attention to the effects of perpendicular E-field on the electronic properties. The electronic band structure of MLG/PHS as function of E-field parallel and anti-parallel to the z-axis with considering SOC is shown in Fig. 7(a). The positive (E-field >0) and negative (E-field <0), denotes parallel and anti-parallel to the z-axis respectively. The strength of E-field is from -0.8 V/Å to +0.8V/Å . We found that, with the application of an electric field, the electronic structure is strongly modified. One can observe that with increasing electric field from 0.0 to 0.6 V/Å, band gap will decrease from 160 to 20 meV and it continuously reach to negligible 10 meV at critical value of 0.7 V/Å. With different situation, as the electric field increases larger that 0.7 V/Å, the band gap will increase and reach up to 160 meV band gap at critical value 1.4 V/Å. One can find from Fig. 7(a) that the applying an E-field can shift the Dirac cone of graphene to higher or lower binding energy. By applying positive electric field, the Dirac cone of graphene tends to shift upward to above the Fermi-level. On the contrary, negative E-field leads to move downward the Dirac cone of graphene to below the Fermi level. The nature of this shift is related to the charge transfer between graphene and PHS. In the case of the positive E-field, electrons are mainly transferred from graphene layer to the PHS layer, resulting in the formation of the hole doping. Whereas, in the case of the negative E-field, it is obvious that the transportation of the electrons is flowed from valence band of the PHS layer to the graphene layer, forming the electron doping. This observation was also confirmed by experiments in other graphene-based heterostructurs[68]. More interestingly, it should be noted that the charge carrier (N) (for electrons and for holes) increases with increasing the shift of graphene Dirac cone by $\Delta E_F = \hbar\, v_F \sqrt{N\pi}$. Therefore, from above discussed, we find that the positive E-field tends to an increase in the charge carrier of hole doping, whereas the negative E-field leads to an increase in the charge carrier of electron doping.

Strain engineering is a robust method to tune the electronic properties and the topological nature and thus it is interesting to investigate this effect. Out-of plane strain, i. e. pressure, can change the interlayer distance and thus the vdW interaction, which may induce electronic state transitions. Here, we investigate the effect of in-plan strain on the electronic properties of LG/PHS. The effects of the interlayer couplings on the electronic properties of LG/PHS are depicted in Fig. 7(b). It is obvious that the interlayer coupling can modify strongly the electronic properties.

One can find that the interlayer coupling can not only tune the band gap of PHS part,but also shift the Dirac cone of graphene part to lower or higher binding energy. When the interlayer coupling is weakened, i.e the interlayer distance is increased, the SOC

View Article Online
DOI: 10.1039/D0TA02847A

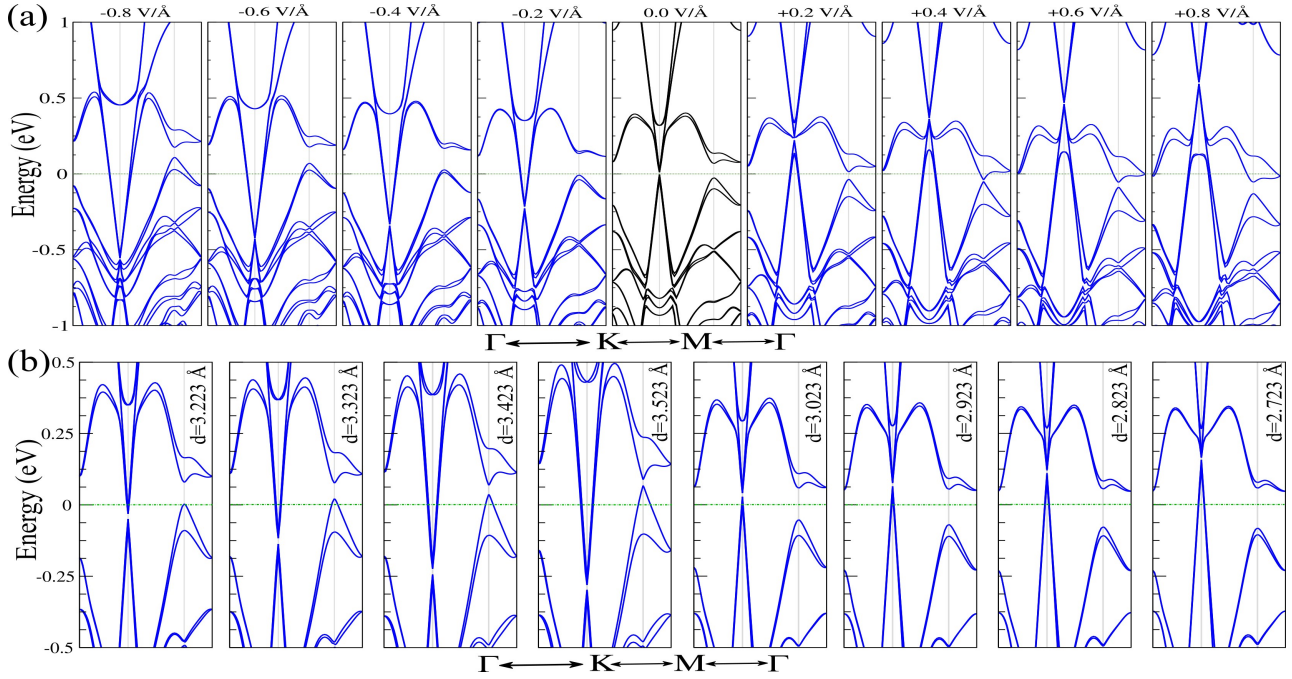

Fig. 7 Electronic band structure of MLG/PHS as function of (a) electric field and (b) interlayer distance with considering SOC. The perpendicular electric field is parallel to the z-axis. The zero of energy is set at Fermi-level.

band gap of PHS is decreased. More interestingly, the weakened interlayer coupling shifts the Dirac cone of graphene to lower binding energy, resulting in the formation of electron doping in graphene. Therefore, the charge carrier of electron doping in graphene is also increased with increasing interlayer distance. In contrast, when the interlayer coupling is strengthened, i.e the interlayer distance is decreased, one can observe that the SOC band gap of PHS part in the LG/PHS is increased. Moreover, the Dirac cone of graphene in LG/PHS moves to above the Fermi level, i.e to higher binding energy, leading to the formation of the hole doping. With decreasing the interlayer distance, it is obvious that the the charge carrier of hole doping also increases. Therefore, we can conclude that the electric field and interlayer coupling can tune the SOC band gap of PHS and induce switchable doping in graphene, leading to enhance the charge carrier of electron and hole doping of LG/PHS.

6 Optical properties

Photoelectric heterostructure materials are expected to absorb as much visible light in order to achieve an efficient electric current conversion[69,70]. Thus, the optical properties of graphene, PHS and LG/PHS are studied based on the results of imaginary and real parts of the dielectric functions ($\varepsilon(\omega)$), refractive index (n), optical conductivity (σ), extinction coefficient (K), electron loss (L), reflectivity (R), and optical absorption spectra, as shown in Fig. 8. The frequency-dependent complex dielectric functions $\varepsilon(\omega) = \varepsilon_1(\omega) + i\varepsilon_2(\omega)$ are calculated. The imaginary part ε_2 can be derived from a summation over a satisfactorily large number of empty states, and the real part ε_1 is realized from the imaginary one by Kramer-Kronig relation, respectively. The derivative of other optical features can be found in detailed elsewhere[72] and also the real part of the dielectric function signifies the storage of energy of a solid[73].

The photo-response features of the MLG/PHS were extended to cover most of the UV and visible ranges. Interestingly, the absorption intensity of the constructed heterostructure is stronger than that of individual PHS and graphene. Thus, MLG/PHS can absorb UV-vis light more efficiently. Increasing the number of graphene layers has a positive impact on the UV-vis light absorption. A clear red-shift with enhanced absorption intensity is observed for BLG/PHS and TLG/PHS configurations, see Fig. 8(a). It can be established that the constructed heterostructures hold the distinctive optical features of individual PHS monolayer and graphene, and also show some exceptional optical characteristics, like the distinctive dielectric function, enhanced absorption intensity, the absorption spectrum in the visible light range and the wide range of photo-response, which indicates promising applications in photo-electric and optical transmission devices.

As shown in Fig. 8(b), the optical conductivity has several peaks, started from the visible region and reaches maximum values at the UV region. The maximum optical conductivity for MLG/PHS is $\sim$ 4.12 at 12.5 eV and reaches approximately zero at higher energies. The peaks of the constructed heterostructures are slightly red-shifted with enhanced intensity as compared to that of the pristine monolayers. The high light responsivity and improved conductive of Pt2HgSe3/Graphene hetero-multilayers, make them suitable for photodetectors applications[74] Similar to the refractive index, the extinction coefficients spectra have several peaks located in the UV-Vis range, see Fig. 8(c). This indicates that there are a number of transitions between the valence and conduction bands. As presented in Fig. 8(d), the $\varepsilon_2(\omega)$ spectrum of PHS demonstrates an absorption peak in the visi-

View Article Online
DOI: 10.1039/D0TA02847A

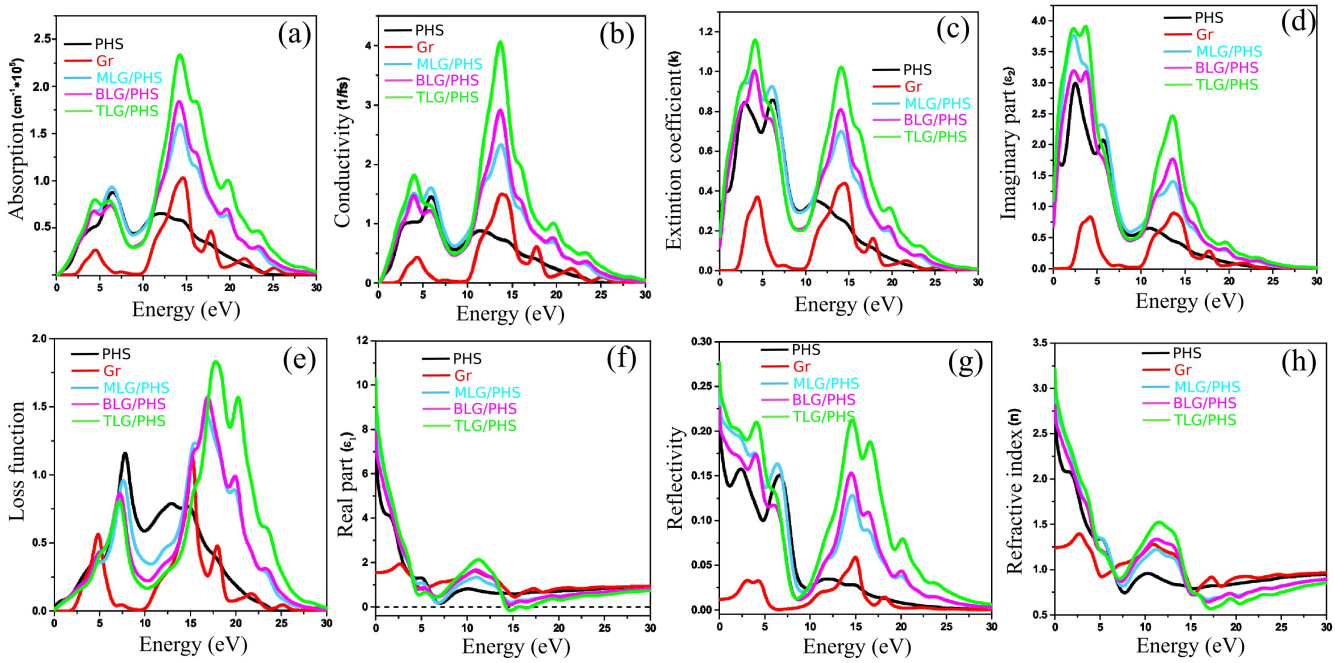

Fig. 8 Optical properties of *PHS*, graphene, and *MLG*/*PHS*, *BLG*/*PHS*, and *TLG*/*PHS* including: (a) optical absorption spectra, (b) optical conductivity (σ), (c) extinction coefficient (K), (d) imaginary and real parts of the dielectric function ($\varepsilon(\omega_2)$), (e) electron loss (L), (f) real part of the dielectric function ($\varepsilon(\omega_1)$), (g) reflectivity (R), (h) refractive index (n).

ble region ($<$ 2.5 eV), indicating that *PHS* could absorb more visible light. The obtained results are in good agreement with similar compounds[76]. In the meantime, the $\varepsilon_2(\omega)$ spectrum of the graphene is reduced as compared to that of *PHS*, indicating that graphene has a somewhat weak absorption capability for *UV* and visible light. The obtained spectrum is matched well with that of experimental observation[77]. Indeed, each peak in the spectrum of the imaginary part can be assigned to an interband transition. The $\varepsilon_2(\omega)$ spectra of the constructed hetrostrucutres signify three optical transitions of filled levels to empty ones (2.4 eV, 4.8 eV, and 6.1 eV). These transitions of the interbands occur from valence band to conduction one along the high symmetry directions. For *PHS*, the maximum energy loss function $L(\omega)$ in the low energy zone reaches 1.25, while that of graphene is about 0.6 (see Fig. 8(e)).

For *PHS* monolayer, the maximum energy loss reaches 1.25 at 7.5 eV, while that of graphene is about 0.6 at 4.8 eV. The energy loss values of the constructed heterostructures are between 0.8 and 0.9, which are comparable to that of graphene. The energy loss spectra of the individual monolayers and the constructed heterostructures are increased with the increase of energy. It is noticeable that the constructed multilayer heterostrucutres have no loss or very small in the *IR* and visible regions. At high photon energy, the energy loss spectra are blue-shifted compared to that of the bare monolayers. The peaks of the imaginary part of the dielectric function and the loss spectra at along photon energies can represent the Plasmon oscillations. Surface and volume Plasmon oscillations can be easily distinguished from loss spectra. At energy range between 4.8-8 eV, surface Plasmon is occurred for both the heterotrouctures and monolauers, while volume Plasmon oscillation is observed at higher energyies ($>$ 15 eV).

At high photon energy, the energy loss spectra are blue-shifted compared to that of the pristine monolayers. As shown in Fig. 8(f), the calculated values of $\varepsilon_1(0)$ for *PHS* and graphene are 6.44 and 1.56, respectively. The obtained results are in good agreement with previous theoretical calculation[75]. After *PHS*-graphene contact, $\varepsilon_0(\omega)$ value has been significantly increased to reach a value of 8.12, which indicates the semiconductivity of this compound. The $\varepsilon_1(0)$ value of graphene-*PHS* contact, has been significantly increased. It can be seen that the *TLG*/*PHS* configuration has a negative value of $\varepsilon_1(\omega)$ at $\sim$15 eV, indicating the metallic nature of this configuration. The $R(\omega)$ spectra of the individual monolayers and heterostructures are presented in Fig. 8(g). For graphene, the reflectivity starts from 0.012, which is the maximum value of R that occurs at zero photon energy. The R value is significantly increased for *PHS* as well as for constructed heterostructures. One may observe that the reflectivity of the constructed heterostructures is higher than that of the individual monolayers. The reflectivity is decreased with increasing energy up to 7.5 eV and again increases in the edges at 10 eV and lastly goes near zero at higher energies. The optical conductivity (σ) is another important parameter that can be used to characterize the optical properties of 2DM[78].

Fig. 8(h) shows the refractive index (n) of the individual monolayers and the studied heterostructures. Penns model[79] describes that $\varepsilon_0(\omega)$ depends on bandgap of a material and $\varepsilon_0(\omega)$ is directly correlated to the static refractive index $n(0)$, which is expressed as $n(0) = \sqrt{\varepsilon_0(\omega)}$ The static refractive indices $n(0)$ for *PHS* and graphene are calculated to be 2.53 and 1.24, respectively. The value of $n(0)$ for *MLG*/*PHS* is noticeably increased and reached to 2.85. Increasing the numbers of graphene layers has a positive impact on the $n(\omega)$ spectra of *MLG*/*PHS*. For

View Article Online
DOI: 10.1039/D0TA02847A

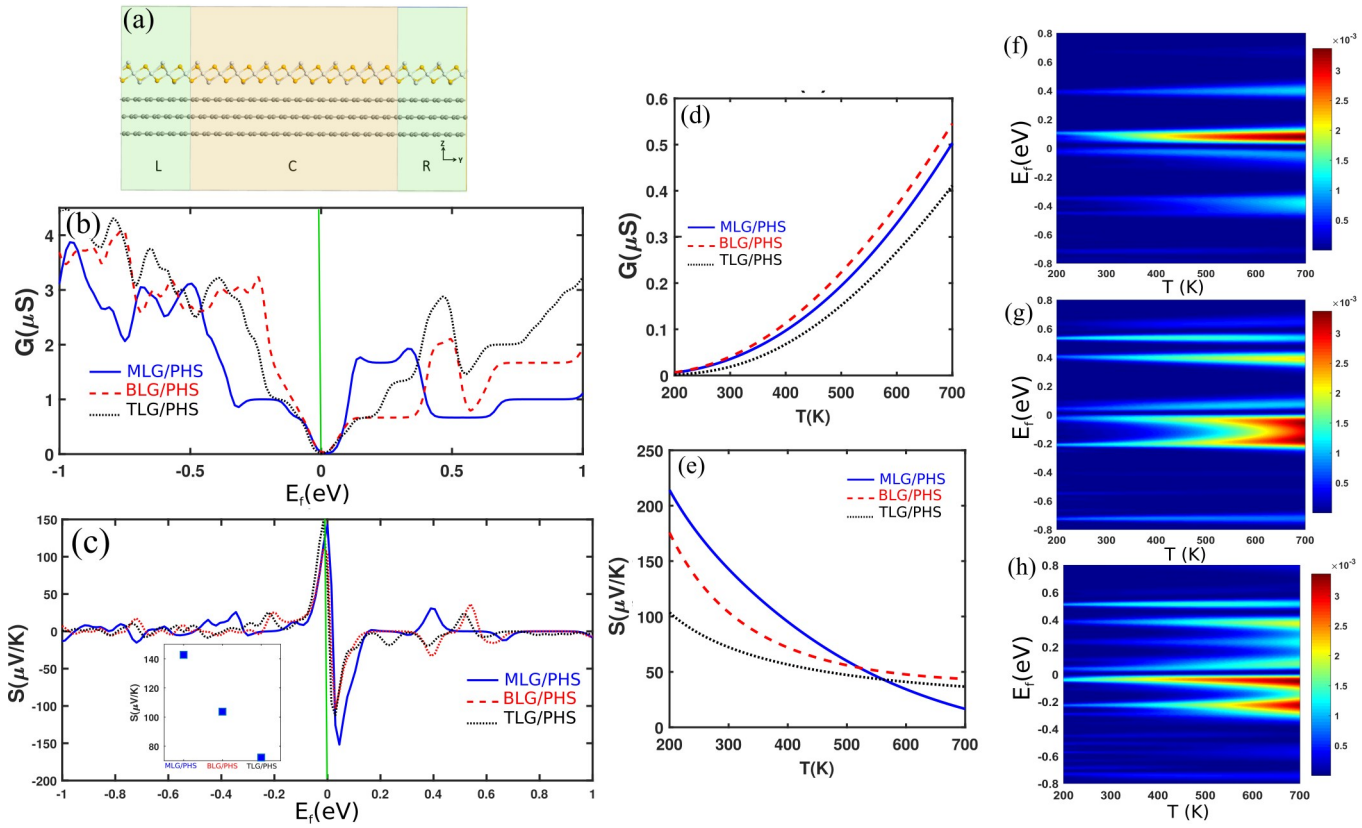

Fig. 9 (a) Electronic device composed of trilayer graphene and PHS monolayer. L (R) and C denotes left (right) electrode and central region, respectively. Electron transport is along Y-direction while the layers are stacked along Z-direction. (b) and (c) electrical conductance and thermopower at room temperature for different thicknesses of graphene. (d) Electrical conductance and (e) thermopower of the heterostructure versus temperature at the Fermi-level. Power factor as a function of temperature and chemical potential for (f) MLG/PHS, (g) BLG/PHS, and (h) TLG/PHS. The power factor is in unit of pW/k^2.

energy between 0 and 15 eV, the refractive indices of BLG/PHS and TLG/PHS are higher than that of MLG/PHS. The refraction index amplitude decreases abruptly so that after 15 eV, the refraction index becomes less than one. In this case, constructed heterostrucutres play the role of an accelerator for the light, and the speed of light in the material exceeds the speed of light in the vacuum representing the superluminal phenomenon.

7 Thermoelectric properties

Fig. 9(a) shows an electronic device composed of graphene trilayer and PHS monolayer. Due to symmetry of the structure, we just consider the transport phenomena along Y-direction. The device is constructed from left and right electrodes and a central region. The transport is considered to be ballistic and inelastic scatterings are ignored. Electronic conductance for different layers of graphene as a substrate is shown in Fig.9(b). At the Fermi-level, the conductance is low due to the Dirac point observed in the band structure of the heterostructure. The electrical conductance can sharply change with lowering the Fermi level possible by gating or p-doping in the experiment. Dependence of G on the thickness of the graphene is complicated. Although it is higher for monolayer graphene in n-doping, bilayer graphene induces higher electrical conductance in p-doping. The electrical conductance in the structure with trilayer graphene is more symmetric than others coming from symmetry of the band structure around Γ. Fig.9(c) reveals dependence of the thermopower on the thickness of the graphene layer. Rate of reduction is more intense for monolayer graphene so that the thermopower possess the lowest value for that at high temperatures. Dependence of G at the Fermi-level on the temperature is quadratic as shown in Fig.9(d). The rate of increase is dependent on the thickness so that the bilayer graphene generates higher electrical conductance. Thermopower is dependent on the band structure and its variations. The maximum of thermopower is obtained at the band edges, so the highest value of the thermopower is located around the Fermi-level as shown in Fig.9(e). At the Fermi level where the bands cross each other the thermopower sign is changed. We found that the magnitude of the thermopower at the Fermi-level is linearly reduced by increase of graphene thickness as shown in the inset of Fig.9(e). The maximum magnitude of thermopower obtained in our device is at least two times higher than the value reported for graphene exfoliated on the Si/SiO_2 substrate[80] that showing the positive effect of proximity on the modifying the thermopower. Unlike the electrical conductance, the thermopower is significantly reduced by increase of temperature at the Fermi-level. Our findings about electronic properties of the heterostructure indicate the performance of the device is strongly dependent on the thickness of the graphene layer. Therefore, one

View Article Online
DOI: 10.1039/D0TA02847A

can tune the electronic capability of the device by engineering of the graphene thickness. Power factor, $PF = S^2G$, reveals thermoelectric efficiency of the device. The power factor as a function of temperature and chemical potential for MLG/PHS, BLG/PHS, and TLG/PHS are shown in Figs.9(f-h). Increase of G and reduction of thermopower are competing with each other in high temperatures to control the behavior of the PF. Because the variation slope of G is higher, the PF increases by raising the temperature. Increase of layer thickness brings the highest peak of PF close to the Fermi level. For monolayer graphene, an asymmetry in the PF is attributed to the asymmetry in the electrical conductance around the Fermi level as shown in Fig.9(b). For thicker graphene layers, the PF is significant in $E_f < 0$ that is causing from the enhancement of electrical conductance in p-doping.

8 Conclusion

In summary, we have systematically investigated the structural and electronic properties of Pt_2HgSe_3 (PHS) monolayer along with the effects of the graphene thickness layers on the elecronic, optic, and thermoelectric properties by using first-principles calculations. We find that PHS monolayer possesses structural stability and exhibits topological insulator with the SOC band gap about 160 meV. Furthermore, the formation of the MLG/PHS, BLG/PHS, TLG/PHS and $MLG/PHS/MLG$ heterostructures can tune the SOC band gap of PHS monolayer, open a tiny band gap in graphene, that make these heterostructures promising candidate for high speed electronic nanodevices. More interestingly, the electric gating and out-of plane strain can shift the Dirac cone of graphene in the MLG/PHS heterostructure to the lower or higher binding energy, leading to an increase in the hole or electron doing. Absorption spectrum demonstrates two peaks, which are located around 216 nm (5.74 eV) and protracted to 490 nm (2.53 eV), indicating that PHS could absorb more visible light. Increasing the number of graphene layers on PHS has a positive impact on the UV-Vis light absorption and a clear red-shift with enhanced absorption intensity.

In addition, we made a device from PHS and multilayer graphene and calculated thermopower and electrical conductance using combination of DFT and green function formalism in the linear response regime. Electrical conductance increases quadratic with temperature and the rate of enhancement is dependent on the graphene thickness. In contrast, a linear reduction in the thermopower is observed with increase of the graphene thickness. In addition, increasing of temperature results in the reduction of the thermopower. Such analysis reveals that the heterostructuring not only significantly affect the electronic properties, but they also can be used as an efficient way to modulate the optic and thermoelectric properties.

9 Acknowledgements

This work has supported by the National Research Foundation of Korea(NRF) grant funded by the Korea government(MSIT)(NRF-2017R1A2B2011989) and Vietnam National Foundation for Science and Technology Development (NAFOSTED) under grant number 103.01-2019.05.

References

1 K. S. Novoselov, A. K. Geim, S. V. Morozov, D. Jiang, Y. Zhang, S. V. Dubonos, I. V. Grigorieva, and A. A. Firsov, Electric field effect in atomically thin carbon films, Sci. 306 (2004) 666.

2 Y.-M. Lin, C. Dimitrakopoulos, K. A. Jenkins, D. B. Farmer, H.-Y. Chiu, A. Grill, and P. Avouris, 100-Ghz Transistors from Wafer-Scale Epitaxial Graphene, Sci. 327 (2010) 662.

3 T. Kuila, S. Bose, A. K. Mishra, P. Khanra, N. H. Kim, and J. H. Lee, Chemical functionalization of graphene and its applications, Prog. Mater. Sci. 57 (2012) 1061.

4 A. C. Neto, F. Guinea, N. M. Peres, K. S. Novoselov, and A. K. Geim, The electronic properties of graphene, Rev. Mod. Phys. 81 (2009) 109.

5 L. Banszerus, M. Schmitz, S. Engels, J. Dauber, M. Oellers, F. Haupt, K. Watanabe, T. Taniguchi, B. Beschoten, and C. Stampfer, Ultrahigh-mobility graphene devices from chemical vapor deposition on reusable copper, Sci. Adv. 1 (2015) e1500222.

6 B. Zhan, C. Li, J. Yang, G. Jenkins, W. Huang, and X. Dong, Graphene field-effect transistor and its application for electronic sensing Small 10 (2014) 4042.

7 F. Xia, T. Mueller, Y.-m. Lin, A. Valdes-Garcia, and P. Avouris, Ultrafast graphene photodetector, Nat. Nanotechnol. 4 (2009) 839.

8 M. S. Jang, H. Kim, Y.-W. Son, H. A. Atwater, and W. A. Goddard, Graphene field effect transistor without an energy gap, Proc. Nat. Acad. Sci. 110 (2013) 8786.

9 M. Xu, T. Liang, M. Shi, and H. Chen, Graphene-Like Two-Dimensional Materials, Chem. Rev. 113 (2013) 3766.

10 G. R. Bhimanapati, Z. Lin, V. Meunier, Y. Jung, J. Cha, S. Das, D. Xiao, Y. Son, M. S. Strano, V. R. Cooper, et al., Recent Advances in Two-Dimensional Materials beyond Graphene, ACS Nano 9 (2015) 11509.

11 S. Manzeli, D. Ovchinnikov, D. Pasquier, O. V. Yazyev, and A. Kis, 2D transition metal dichalcogenides, Nat. Rev. Mater. 2 (2017) 17033.

12 Q. H. Wang, K. Kalantar-Zadeh, A. Kis, J. N. Coleman, and M. S. Strano, Electronics and optoelectronics of two-dimensional transition metal dichalcogenides, Nat. Nanotechnol. 7 (2012) 699.

13 A. Carvalho, M. Wang, X. Zhu, A. S. Rodin, H. Su, and A. H. C. Neto, Nat. Rev. Mater. 1 (2016) 1.

14 Ismail Shahid, Sheraz Ahmad, Nasir Shehzad, Sai Yao, Chuong V. Nguyen, Lixin Zhang, Zhen Zhou, Electronic and photocatalytic performance of boron phosphide-blue phosphorene vdW heterostructures Appl. Surf. Sci. 523 (2020) 146483.

15 P. Vogt, P. De Padova, C. Quaresima, J. Avila, E. Frantzeskakis, M. C. Asensio, A. Resta, B. Ealet, and G. Le Lay, Silicene: Compelling Experimental Evidence for Graphenelike Two-Dimensional Silicon, Phys. Rev. Lett. 108 (2012) 155501.

16 J. Tucek, P. Blonski, J. Ugolotti, A. K. Swain, T. Enoki, and R. Zboril, Emerging chemical strategies for imprinting magnetism in graphene and related 2D materials for spintronic

View Article Online
DOI: 10.1039/D0TA02847A

and biomedical applications, Chem. Soc. Rev. 47 (2018) 3899.

17 W. Han, Perspectives for spintronics in 2D materials, APL Mater. 4 (2016) 032401.

18 K. Pham, N. Hieu, H. Phuc, I. Fedorov, C. Duque, B. Amin, and C. V. Nguyen, Layered graphene/GaS van der Waals heterostructure: Controlling the electronic properties and Schottky barrier by vertical strain, Appl. Phys. Lett. 113 (2018) 171605.

19 A. Cabral, H. Galbiatti, R. Kwitko-Ribeiro, and B. Lehmann, Phosphorene: from theory to applications, Terra Nova 20 (2008) 32.

20 A. Vymazalova, F. Laufek, M. Drabek, A. R. Cabral, J. Haloda, T. Sidorinova, B. Lehmann, H. F. Galbiatti, and J. Drahokoupil, Jacutingaite, Pt_2HgSe_3, A new platinum-group mineral species from the caue iron-ore deposit, Can. Mineral. 50 (2012) 431.

21 A. Marrazzo, M. Gibertini, D. Campi, N. Mounet, and N. Marzari, Prediction of a Large-Gap and Switchable Kane-Mele Quantum Spin Hall Insulator, Phys. Rev. Lett. 120 (2018) 117701.

22 X. Wu, M. Fink, W. Hanke, R. Thomale, and D. Di Sante, Unconventional superconductivity in a doped quantum spin Hall insulator, Phys. Rev. B 100 (2019) 041117.

23 K. Kandrai, G. Kukucska, P. Vancso, J. Koltai, G. Baranka, Z. E. Horvath, A. Hoffmann, A. Vymazalova, L. Tapaszto, and P. Nemes-Incze, Evidence for room temperature quantum spin Hall state in the layered mineral jacutingaite, arXiv preprint arXiv:1903.02458 (2019).

24 Z. Dai, L. Liu, and Z. Zhang, Strain Engineering of 2D Materials: Issues and Opportunities at the Interface, Adv. Mater. 31 (2019) 1805417.

25 G. H. Ahn, M. Amani, H. Rasool, D.-H. Lien, J. P. Mastandrea, J. W. Ager III, M. Dubey, D. C. Chrzan, A. M. Minor, and A. Javey, Strain-engineered growth of two-dimensional materials, Nat. Commun. 8 (2017) 1.

26 Z. H. Ni, T. Yu, Y. H. Lu, Y. Y. Wang, Y. P. Feng, and Z. X. Shen, Uniaxial strain on graphene: Raman spectroscopy study and band-gap opening, ACS Nano 2 (2008) 2301.

27 E. J. Santos, in Exotic Properties of Carbon Nanomatter (2015) 383âĂŞ391.

28 G. Giovannetti, P. A. Khomyakov, G. Brocks, P. J. Kelly, and J. Van Den Brink, Substrate-induced band gap in graphene on hexagonal boron nitride: Ab initio density functional calculations, Phys. Rev. B 76 (2007) 073103.

29 J. E. Padilha, R. B. Pontes, and A. Fazzio, Bilayer graphene on h-BN substrate: investigating the breakdown voltage and tuning the bandgap by electric field, J. Phys. Condens. Matter 24 (2012) 075301.

30 K. Novoselov, A. Mishchenko, A. Carvalho, and A. C. Neto, 2D materials and van der Waals heterostructures, Sci. 353 (2016) aac9439.

31 Y. Liu, N. O. Weiss, X. Duan, H.-C. Cheng, Y. Huang, and X. Duan, Few-layer molybdenum disulfide transistors and circuits for high-speed flexible electronics, Nat. Rev. Mater. 1 (2016) 1.

32 C. Li, Q. Cao, F. Wang, Y. Xiao, Y. Li, J.-J. Delaunay, and H. Zhu, Engineering graphene and TMDs based van der Waals heterostructures for photovoltaic and photoelectrochemical solar energy conversion, Chemical Society Reviews 47 (2018) 4981.

33 Y. Li, C.-Y. Xu, J.-K. Qin, W. Feng, J.-Y. Wang, S. Zhang, L.-P. Ma, J. Cao, P. A. Hu, W. Ren, et al., Tuning the Excitonic States in MoS_2/Graphene van der Waals Heterostructures via Electrochemical Gating, Adv. Func. Mater. 26 (2016) 293.

34 K. D. Pham, N. N. Hieu, H. V. Phuc, I. Fedorov, C. Duque, B. Amin, and C. V. Nguyen, A water splitting photocatalysis: Blue phosphorus/g-GeC van der Waals heterostructure, Appl. Phys. Lett. 113 (2018) 171605.

35 Z. Ben Aziza, H. Henck, D. Pierucci, M. G. Silly, E. Lhuillier, G. Patriarche, F. Sirotti, M. Eddrief, and A. Ouerghi, van der Waals Epitaxy of GaSe/Graphene Heterostructure: Electronic and Interfacial Properties, ACS nano 10 (2016) 9679.

36 H. V. Phuc, N. N. Hieu, B. D. Hoi, and C. V. Nguyen, Phys. Chem. Chem. Phys. 20 (2018) 17899.

37 Z. B. Aziza, D. Pierucci, H. Henck, M. G. Silly, C. David, M. Yoon, F. Sirotti, K. Xiao, M. Eddrief, J.-C. Girard, et al., Interlayer coupling and electric field tunable electronic properties and Schottky barrier in a graphene/bilayer-GaSe van der Waals heterostructure, Phys. Rev. B 96 (2017) 035407.

38 H. V. Phuc, V. V. Ilyasov, N. N. Hieu, and C. V. Nguyen, Electric-field tunable electronic properties and Schottky contact of graphene/phosphorene heterostructure, Vacuum 149 (2018) 231.

39 J. Padilha, A. Fazzio, and A. J. da Silva, van der Waals Heterostructure of Phosphorene and Graphene: Tuning the Schottky Barrier and Doping by Electrostatic Gating, Phys. rev. lett. 114 (2015) 066803.

40 A. Bafekry, C. Stampfl, M. Ghergherehchi, S. Farjami Shayesteh, Exploring of novel electronic and magnetic properties in the C_2N nanosheet via defect/strain engineering and impurity of atom. CARBON, 157, 371-384 (2020). DOI:10.1016/j.carbon.2019.10.038

41 A. Bafekry, C. Stampfl, M. Ghergherehchi, and F. M. Peeters, The electronic, optical and thermoelectric properties of monolayer PbTe and the tunability of the electronic structure by external fields and defects. Phys. Status Solidi b âĂŞ Basic Solid State Physics, (2020), DOI:10.1002/pssb.202000182

42 A. Bafekry, M. Neek-Amal, F. M. Peeters, Two-dimensional graphitic carbon nitrides: Strain-tunable ferromagnetic ordering. Phys. Rev. B, 16 (2020) 165407. DOI:10.1103/PhysRevB.101.165407

43 A. Bafekry, B. Akgenc, M. Ghergherehchi and F. M. Peeters, Strain and electric field tuning of semi-metallic character $WCrCO_2$ MXenes with dual narrow band gap. J. Phys.: Condensed Matter, (2020), DOI:10.1088/1361-648X/ab8e88

44 A. Bafekry, M. Ghergherehchi, S. Farjami Shayesteh. and F. M. Peeters. Tuning the band gap and introducing magnetism into BC_3 nanosheet via stain/defect engineering and adatom/molecule adsorption, Appl. Phys., 126 (2019),

View Article Online
DOI: 10.1039/D0TA02847A

144304. DOI:10.1063/1.5097264

45 A. Bafekry, C. Stampfl and S. Farjami Shayesteh, A first-principles study of C_3N nanostructures: Control and engineering of the electronic and magnetic properties of nanosheets, tubes and ribbons, Journal of ChemPhysChem, 2020, 21, 164. DOI:10.1002/cphc.201900852

46 A. Bafekry, S. Farjami Shayesteh and F. M. Peeters, Two-Dimensional Carbon Nitride (2DCN) Nanosheets: Tuning of Novel Electronic and Magnetic Properties by Hydrogenation, Atom Substitution and Defect Engineering. Appl. Phys., (2019) 126, 215104. DOI:10.1063/1.5120525@jap.2020.DIS2020.issue-1

47 A. Bafekry, Gaphen-like BC_6N nanosheet: Tuning of the electronic and magnetic properties via layer thickness, external fields, typical defects and adsorption/substitution of atoms. J. Phy. E: Low-dimen. Sys. Nanost., 113850, 2019. DOI:10.1016/j.physe.2019.113850

48 A. Bafekry, C. Stampfl, F. M. Peeters, Dirac half-metallicity of Thin $PdCl_3$ Nanosheets: Investigation of the Effects of External Fields, Surface Adsorption and Defect Engineering on the Electronic and Magnetic Properties. Sci. rep., 213 (2020). DOI:10.1038/s41598-019-57353-3

49 A. Bafekry, B. Akgenc, C. Stampfl, M. Ghergherehchi, Control of C_3N_4 and C_4N_3 carbon nitride nanosheets' electronic and magnetic properties through embedded atoms. Physical Chemistry Chemical Physics, 22 (2020) 2249-2261.

50 A. Bafekry, M. Ghergherehchi, S. Farjami Shayesteh, Tuning the electronic and magnetic properties of antimonene nanosheets via point defects and external fields: first-principles calculations. Phys. Chem. Chem. Phys., 21 (2019), 10552-10566. DOI:10.1039/C9CP01378D

51 T. Ozaki, K. Nishio, H. Kino, Efficient implementation of the nonequilibrium Green function method for electronic transport calculations Phys. Rev. B 81 (2010) 035116.

52 N. Troullier, J. Martins, Efficient pseudopotentials for plane-wave calculations, Phys. Rev. B 43 (1991) 1993-2006.

53 Variationally optimized atomic orbitals for large-scale electronic structures, T. Ozaki, Phys. Rev. B 67 (2003) 155108.

54 T. Ozaki and H. Kino, Numerical atomic basis orbitals from H to Kr, Phys. Rev. B 69 (2004) 195113.

55 J. P. Perdew, K. Burke and M. Ernzerhof, Generalized Gradient Approximation Made Simple, Phys. Rev. Lett. 77 (1996) 3865-3868.

56 H. J. Monkhorst and J. D. Pack, Special points for Brillouin-zone integrations, Phys. Rev. B 13 (1976) 5188-5192.

57 T. Bucko, J. Hafner, S. Lebegue and J. G. Angyan, Improved Description of the Structure of Molecular and Layered Crystals: Ab Initio DFT Calculations with van der Waals Corrections, J. Phys. Chem. A 114 (2010) 11814-11824.

58 Jose M Soler, E. Artacho, J. D. Gale, A. Garcia, J. Junquera, P. Ordejon and D. Sanchez-Portal, The SIESTA method for ab initio order-N materials simulation, J. Phys.: Condensed Matter 14 (2002) 2745.

59 PHON: A program to calculate phonons using the small displacement method, Alfè, Dario, Computer Physics Communications, 180 ,2622–2633 2009.

60 A. K. Geim, and K. S. Novoselov. The rise of graphene. Nat. mater. **6**, 183 (2007).

61 C. Xia, J. Du, L. Fang, X. Li, X. Zhao, X. Song, T. Wang, J. Li. $PtSe_2$/graphene hetero-multilayer: gate-tunable Schottky barrier height and contact type. Nanotechnology, 29 (2018) 465707.

62 Z. Guan, S. Ni, and S. Hu, Band gap opening of graphene by forming a graphene/$PtSe_2$ van der Waals heterojunction. RSC advances, 7 (2017) 45393-45399.

63 K. Ishizaka, M. S. Bahramy, H. Murakawa, M. Sakano, T. Shimojima, T. Sonobe, K. Koizumi, S. Shin, H. Miyahara, A. Kimura, K. Miyamoto, T. Okuda, H. Namatame, M. Taniguchi, R. Arita, N. Nagaosa, K. Kobayashi, Y. Murakami, R. Kumai, Y. Kaneko, Y. Onose and Y. Tokura, Giant Rashba-type spin splitting in bulk BiTeI. Nature Materials, 10 (2011) 521-526. RSC advances, 7 (2017) 45393-45399.

64 A. Bafekry, B. Akgenc, S. Farjami Shayesteh and B. Mortazavi, Tunable electronic and magnetic properties of graphene/carbon-nitride van der Waals heterostructures. Appl. Surf. Sci., (2019) 144450, DOI:10.1016/j.apsusc.2019.144450

65 A. Bafekry, and M. Neek-Amal, Tuning the electronic properties of graphene-graphitic carbon nitride heterostructures and heterojunctions by using electric field. Phys. Rev. B. 101, (2020) 085417. DOI:10.1103/PhysRevB.101.085417

66 A. Bafekry, M. Yagmurcukardes, B. Akgenc, M. Ghergherehchi and Ch. V Neguyen Van der Waals heterostructures of layered Janus transition-metal dichalcogenides (MoS_2 and Janus MoSSe) on graphitic boron-carbon-nitride (BC_3, C_3N, C_3N_4 and C_4N_3) nanosheets: A First-Principles study. J. Phy. D: Appl. Phys., (2020) DOI:10.1088/1361-6463/ab876c

67 A. Bafekry, C. Stampfl and M. Ghergherehchi, Strain, electric-field and functionalization induced widely tunable electronic properties in MoS_2/BC_3, $/C_3N$ and $/C_3N_4$ van der Waals heterostructures. Nanotechnology, (2020) DOI:10.1088/1361-6528/ab884e

68 Z. B. Aziza, H. Henck, D. Pierucci, M. G. Silly, E. Lhuillier, G. Patriarche, F. Sirotti, M. Eddrief, A. Ouerghi, van der Waals Epitaxy of GaSe/Graphene Heterostructure: Electronic and Interfacial Properties ACS Nano 10 (2016) 9679-9686.

69 S.E. Tsoeu,F. Opoku, and P.P. Govender, Tuning the electronic, optical and structural properties of GaS/C_2N van der Waals heterostructure for photovoltaic application: first-principle calculations. SN Applied Sciences 2 (2020) 341.

70 M.M Obeid, Tuning the electronic and optical properties of Type-I PbI_2/Îś-tellurene van der Waals heterostructure via biaxial strain and external electric field. Appl. Surf. Sci. 508 (2020) 144824.

71 Y. Bai, Q. Zhang, N. Xu, K. Deng, E. Kan, Efficient carrier separation and band structure tuning of two-dimensional C_2N/GaTe van der Waals heterostructure. Phys. Chem. C 122 (2018) 15892-15902.

72 H.R. Jappor and M.A. Habeeb, Optical properties of two-

View Article Online
DOI: 10.1039/D0TA02847A

dimensional GaS and GaSe monolayers. Physica E: Low-dimensional Systems and Nanostructures, 101 (2018) 251-255.

73 M. Ahmad, G. Rehman, L. Ali, M. Shafiq, R. Iqbal, R. Ahmad, T. Khan, S. Jalali-Asadabadi, M. Maqbool and I. Ahmad, Structural, electronic and optical properties of $CsPbX_3$ (X= Cl, Br, I) for energy storage and hybrid solar cell applications. Journal of Alloys and Compounds 705 (2017) 828-839.

74 H. Qiao, J. Yuan, Z. Xu, C. Chen, Sh. Lin, Y. Wang, J. Song, Y. Liu, Q. Khan, H. Y. Hoh, Ch.-X. Pan, Sh. Li, Q. Bao, Broadband Photodetectors Based on GrapheneâĂŞBi_2Te_3 Heterostructure. ACS Nano 9 (2015) 1886-1894.

75 P. Nath, S. Chowdhury, D. Sanyal and D. Jana, Ab-initio calculation of electronic and optical properties of nitrogen and boron doped graphene nanosheet. Carbon 73 (2014) 275-282.

76 W.-L. Tao, Y. Mu, C.-E. Hu, Y. Cheng, G.-F. Ji, Electronic structure, optical properties, and phonon transport in Janus monolayer PtSSe via first-principles study. Philosophical Magazine 99 (2019) 1025-1040.

77 E. Lepore, F. Bosia, F. Bonaccorso, M. Bruna, S. Taioli, G. Garberoglio, A. C. Ferrari and N. M. Pugno Spider silk reinforced by graphene or carbon nanotubes. 2D Materials 4 (2017) 031013.

78 X. Chen,Q. Yang, R. Meng,J. Jiang, Q. Liang, Ch. Tan, and X. Sun, The electronic and optical properties of novel germanene and antimonene heterostructures. Mater. Chem. C 4 (2016) 5434-5441.

79 D. R. Penn, Wave-Number-Dependent Dielectric Function of Semiconductors. Phys. Rev. 128 (1962) 2093 .

80 G. J. Checkelsky and N. P. Ong. Thermopower and Nernst effect in graphene in a magnetic field Phys. Rev. B 80 (2009) 081413(R).